

RESEARCH ARTICLE | SEPTEMBER 22 2023

Flexible thin film optical solar reflectors with Ta₂O₅-based multimaterial coatings for space radiative cooling

Special Collection: [Photonic Structures for Efficient Thermal Management](#)

Wei Xiao ; Peng Dai ; H. Johnson Singh ; Idris A. Ajia; Xingzhao Yan; Peter R. Wiecha ; Ruomeng Huang ; C. H. (Kees) de Groot ; Otto L. Muskens ; Kai Sun  

 Check for updates

APL Photonics 8, 090802 (2023)
<https://doi.org/10.1063/5.0156526>

 View Online

 Export Citation

 CrossMark

Articles You May Be Interested In

Experimental evidence of multimaterial jet formation with lasers


Phys. Plasmas (November 2010)

Multimaterial direct energy deposition: From three-dimensionally graded components to rapid alloy development for advanced materials

J. Laser Appl. (December 2022)

Sound transmission loss improvement using additively manufactured multimaterial

Proc. Mtgs. Acoust. (October 2022)



THE ADVANCED MATERIALS MANUFACTURER®

yttrium iron garnet glassy carbon beamsplitters fused quartz additive manufacturing

zeolites III-IV semiconductors gallium lump copper nanoparticles organometallics

nano ribbons barium fluoride europium phosphors photonics infrared dyes

sapphire windows Nd:YAG epitaxial crystal growth ultra high purity materials transparent ceramics CIGS

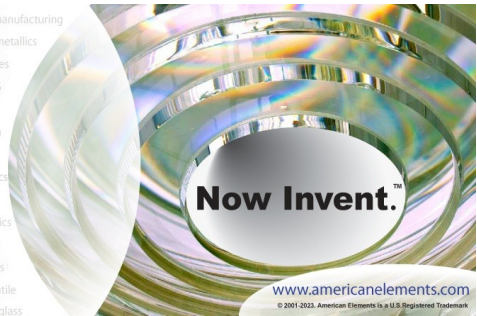
spintronics raman substrates cerium oxide polishing powder surface functionalized nanoparticles cermet nanodispersions

silver nanoparticles perovskites MOCVD beta-barium borate rare earth metals quantum dots osmium scintillation Ce:YAG refractory metals laser crystals anodic titanium niobate InAs wafers

perovskite crystals transparent ceramics ZnS CdTe MOFs AuNPs Ti Pa U Np Pu Am Cm Bk Cf Es Fm Md No Lr Ce Pr Nd Pm Sm Eu Gd Tb Dy Ho Er Tm Yb Lu Th Pa U Np Pu Am Cm Bk Cf Es Fm Md No Lr

YBCO superconductors InGaAs indium tin oxide MgF₂ rutile optical glass

metamaterials borosilicate glass diamond micropowder



Now Invent.™

www.americanelements.com

© 2001-2022, American Elements LLC, a U.S. Registered Trademark.

The Next Generation of Material Science Catalogs

Flexible thin film optical solar reflectors with Ta₂O₅-based multimaterial coatings for space radiative cooling

Cite as: APL Photon. 8, 090802 (2023); doi: 10.1063/5.0156526

Submitted: 30 April 2023 • Accepted: 4 September 2023 •

Published Online: 22 September 2023



View Online



Export Citation



CrossMark

Wei Xiao,^{1,2} Peng Dai,² H. Johnson Singh,¹ Idris A. Ajia,¹ Xingzhao Yan,³ Peter R. Wiecha,⁴ Ruomeng Huang,² C. H. (Kees) de Groot,² Otto L. Muskens,¹ and Kai Sun^{1,2,a)}

AFFILIATIONS

¹School of Physics and Astronomy, Faculty of Engineering and Physical Sciences, University of Southampton, Southampton SO17 1BJ, United Kingdom

²Electronics and Computer Science, Faculty of Engineering and Physical Sciences, University of Southampton, Southampton SO17 1BJ, United Kingdom

³Optoelectronics Research Centre, Zepler Institute for Photonics and Nanoelectronics, Faculty of Engineering and Physical Sciences, University of Southampton, Southampton SO17 1BJ, United Kingdom

⁴LAAS-CNRS, Université de Toulouse, 31000 Toulouse, France

Note: This paper is part of the APL Photonics Special Topic on Photonic Structures for Efficient Thermal Management.

a) Author to whom correspondence should be addressed: k.sun@soton.ac.uk

ABSTRACT

Optical Solar Reflectors (OSRs) combine low solar radiation absorption (α) and high broadband infrared emissivity (ϵ) and are applied to the external surface of spacecraft for its thermal management. Bulk glass OSR tiles are the incumbent, but ultra-lightweight and thin-film flexible OSR coatings are raising considerable interest for both space and terrestrial radiative cooling applications. In this work, a genetic algorithm combined with a transfer matrix method is used for the design and optimization of multimaterial thin-film OSRs for broadband radiative cooling. The algorithm simultaneously optimizes the spectral performance of the OSR at two parts of the wavelength spectrum, solar (0.3–2.5 μm) and thermal infrared (2.5–30 μm). The designed optimized OSR structure consists of 18 alternating layers of three materials, SiN, SiO₂, and Ta₂O₅, on top of an Al mirror backreflector, with a total thickness of only 2.088 μm . The optimized multilayer stack contributes distributed Bragg reflections that reduce the residual solar absorption below that of an uncoated Al mirror. The optimized OSR is demonstrated experimentally on a 150 mm (6 in.) Si wafer and on a flexible polyimide substrate using a production level reactive sputtering tool. The fabricated thin film OSR shows good thermal-optical property with $\alpha = 0.11$ and $\epsilon = 0.75$ and achieves a net cooling power of 150.1 W/m² under conditions of one sun total solar irradiance in space. The ultrathin coating fabricated using hard inorganic materials facilitates its integration onto flexible foils and enables large-scale manufacture of low-cost OSRs for broadband radiative cooling applications.

© 2023 Author(s). All article content, except where otherwise noted, is licensed under a Creative Commons Attribution (CC BY) license (<http://creativecommons.org/licenses/by/4.0/>). <https://doi.org/10.1063/5.0156526>

I. INTRODUCTION

During the operation of spacecraft, large variations in the external environment can result in temperature fluctuations between –150 and 150 °C.¹ The spacecraft thermal control system plays a vital role in maintaining survivable conditions for the equipment on board, ensuring the normal operation of the spacecraft's internal

electronics, and extending the service life of the spacecraft.^{2,3} The only way to exchange heat between the spacecraft and space is through thermal radiation at infrared wavelengths.⁴ As one of the most important passive thermal control devices for spacecraft, Optical Solar Reflector (OSR) coatings provide low absorption of incident solar radiation (α) and high broadband infrared emissivity (ϵ). To achieve efficient thermal dissipation for spacecraft, the ratio of

emissivity to absorption of the OSR (ϵ/α) should be high and is typically of the order of 8–16 depending on the type of OSR.^{5–8}

Since the 1960s, the glass-tile based optical solar reflectors (OSRs), also known as secondary surface mirrors, are the main thermal radiators used on spacecraft. The basic structure of these is a 100 nm thin film of aluminum or silver deposited on the side of a borosilicate glass with thickness around 150–200 μm .⁹ These glass tile OSRs are fragile and cannot be bent or folded, and the assembly process is labor intensive and expensive.¹⁰ Flexible OSRs were, therefore, developed, which are predominantly based on slivered fluorinated ethylene propylene (FEP). However, the FEP OSR is well-known to suffer severely degradation under solar irradiation and thermal cycling, making it only suitable for short space missions of 3–5 years.^{11,12} Development of flexible, lightweight, and durable OSR solutions for the radiative cooling of spacecraft is of great interest for application in lightweight spacecraft, large-scale structures, such as space-based solar power systems, starshot lightsails, and future solar sail technology.

In recent years, much effort has been directed toward the development of daytime radiative cooling devices for terrestrial applications.^{13–18} In 2014, a multilayer thin film based radiative cooler was introduced that not only achieved a high solar radiation reflectivity of 97% but also a high infrared emissivity of 60% in the 8–13 μm atmospheric window. This was the first experimental demonstration of daytime radiative cooling and achieved temperatures nearly 5° lower than the ambient environment under direct sunlight.¹⁹ However, several studies have demonstrated high-performance day-time radiative cooling using a diversity of structures, including besides thin film stacks also metasurface designs, with the purpose of cooling applications for terrestrial objects, such as buildings, smart windows, and solar cells.^{20–27}

In comparison to terrestrial applications, demonstrations of thin-film inorganic multimaterial structures for broadband radiative cooling in space have remained limited with some recent efforts directed at conventional Salisbury screen designs and thicker distributed Bragg stacks.^{28–31} Recently, our team has developed meta-surface-based OSRs, based on a Salisbury screen metamaterial perfect absorber geometry and consisting of an Aluminum-doped Zinc Oxide (AZO) metasurface on a SiO₂ dielectric layer on an Al mirror.³² The fabrication of patterned OSRs is relatively expensive due to the complex lithography processes involved, and scaling up involves techniques such as nanoimprint lithography, rendering the high cost compared to unpatterned thin-film structures.

Organic material-based radiative cooling films and radiative cooling paints with porous structures can also achieve broadband infrared absorption, and the simplicity of those techniques could be applied to different surfaces by painting or spraying.^{33,34} However, organic polymer materials based radiative cooling film or paints are generally not suitable for space applications because of the extreme conditions of the radiation environment in outer space, which includes high energy cosmic rays as well as ionizing solar radiation and stronger solar UV radiation.^{3,35–37} Prolonged radiation exposure causes self-oxidation, degradation, and breakage of the polymer's chemical bonds and seriously affects the spacecraft's thermal control capability and ultimately its lifetime.³⁸

Here, we demonstrate the use of optimized inorganic, oxide-based thin-film stacks to achieve broadband radiative cooling surfaces compatible with the requirements for space applications. For

the initial design, we combine a Genetic Algorithm (GA) with the Transfer Matrix Method (TMM) to optimize the thin-film multi-material OSR in both the solar absorptance (0.3–2.5 μm) and the infrared emissivity (2.5–30 μm), with the aim of achieving the maximum ϵ/α for efficient radiative cooling of spacecraft. In our study, the GA optimizes the combination of the total number of layers, the material choice for each layer, and the thickness of each layer. In recent years, the application of machine learning algorithms to accelerate the design and optimization of optical devices and coatings has become an important tool.^{39–42} Evolutionary algorithms have been successfully applied for the optimization of multilayer radiative coolers.^{13,43–49} Those previous studies involved optimization of stacks consisting of two different materials (HfO₂–SiO₂,¹⁹ SiN–SiO₂,⁴⁵ SiN–MgF₂,⁴⁶ or TiO₂–SiO₂⁴⁸) and focused on achieving a high absorption in the atmospheric window (8–13 μm). As we show here, by increasing the number of different materials in the stack beyond two and strategically including materials with absorption at longer wavelengths, we significantly extend the spectral range over which a high emissivity is obtained.

Considering the practical fabrication, the material candidates for the thin film OSR optimization are chosen to be compatible with our reactive sputter deposition system. This ensures that the OSR can be achieved in a one-go manufacturing process without breaking the vacuum state between each layer, which is essential for getting a high-quality film stack. The optimized design of the thin film OSR in this work is made of 18 layers of SiO₂, SiN, and Ta₂O₅, where Ta₂O₅ is introduced for improving the absorption at wavelengths in the range 13–25 μm . The selected thin-film OSR design is experimentally fabricated on both a 150 mm (6 in.) silicon wafer and on a polyimide foil (DuPont Kapton[®] PFC 300) to demonstrate its use in flexible thin-film and ultra-lightweight applications. Here, Kapton PFC 300 is chosen for its high robustness and duration for space environment as demonstrated in the recent EU FIRST-FLEX project by Consorzio CREO. Thus, all dielectric layers, along with an aluminum reflector and polyimide, can withstand temperatures of up to 350 °C, making them suitable for the harsh space environment.

II. MATERIALS AND METHODS

A. Optimization using genetic algorithm

The optimization strategy used in this work is the genetic algorithm (GA), which is based on the principle of natural selection. The main framework of genetic algorithm used is based on DEAP (Distributed Evolutionary Algorithms in Python), which could be used as a groundwork for application of evolutionary algorithms, such as the particle swarm optimization and genetic algorithm.⁵⁰ The GA is used to search the maximum object function in the predefined range with an evaluation function, which is normally to get a maximum or minimum Objective Function/Figure of Merit (FOM), and here, it is to achieve the maximum FOM defined as the ratio of thermal emissivity to solar absorption, ϵ/α . GAs tend to be very useful when the objective function is highly complex or discontinuous. The two most notable advantages of a GA over other optimization algorithms are the capability of dealing with complicated problems and parallelism in the computation.⁵¹ The various offspring in one generation can search the design space in different directions

simultaneously, and this feature offers the GA the advantages of internal parallelism.

The GA was coupled with the Transfer Matrix Method (TMM) to optimize the optical properties, including reflectance, transmittance, and absorbance. The flow chart of the GA for the OSR is shown in Fig. 1(a). The first generation was randomly initialized at the beginning to avoid a local optimum. Each generation consists of a parameter set known as chromosome; different layer thicknesses and layer materials combinations are coded into these chromosomes. The chromosomes were subsequently divided into many subsets, where each subset represents a gene referring to the selected thickness and material parameters. In each optimization cycle, the absorption spectrum of each subset was calculated by TMM through decoding those genes into thickness and materials related parameters. The gene population was optimized (after crossover and mutation phases) and stored according to the quality of the evaluation function; the chromosomes with highest fitness were selected and passed on to the next generation. After the number of the generations reached the predefined value of 100, the optimization was terminated. The crossover and mutation probabilities were set to be 0.8 and 0.2, respectively. The population size of each generation in the GA was set to 100. The total thickness was constrained to below $2.5\ \mu\text{m}$ by setting the maximum number of layers to 25 and the maximum thickness of each layer to 100 nm; constraining the range of thicknesses allows us to maintain the thin-film characteristics of the resulting coatings, such as mechanical flexibility, conformality, and manufacturability. The GA can define thicker layers $>100\ \text{nm}$ by using the same material for two or more adjacent layers in the stack. Below, we present the merged layer structure where adjacent layers of the same material are combined into one layer, thus reducing the effective total number of layers in the stack.

B. Fabrication

Reactive sputtering under high vacuum conditions is used for the optical film coating in a one-go process. As an industrial-level sputtering equipment for the fields of precision optics and optoelectronics, the Bühler Helios sputtering tool provides the capability to load 12 pieces of 200 mm (8 in.) wafer at one time and to process intricate stacked layers in a single run using a programmed recipe, all without breaking the vacuum. Figure 2 represents an illustration of the process. The Helios sputtering tool has two mid-frequency plasma sources (for dielectric sputtering) and one DC source (for metal sputtering). The sputter source is made of two separate sputter electrodes that act as sputter cathodes alternatively. The alternating electrical field for the alternating polarity of the electrodes is provided by the mid-frequency (MF) generator, while the dielectric sputter sources are supplied by the same MF generator and can only operate separately. Each sputter electrode is equipped with a rectangular target, which is bonded on to a copper backing plate and connected with a water-cooled cover; the cover includes a magnetic system for increasing the plasma intensity. Three different targets could be installed, allowing for up to six different compounds and three elements to be deposited with two plasma sources (O_2 or N_2) and the DC source, respectively.

A 150 mm (6 in.) silicon wafer was loaded into the chamber. Then, the 100 nm Al mirror was deposited by utilizing the DC source and Al target; subsequently, 18 alternating layers of Ta_2O_5 , SiO_2 , and SiN were deposited by using mid-frequency plasma sources (O_2 and N_2) and the Si/Ta target. The deposition rates for Ta_2O_5 , SiO_2 , SiN , and Al are 0.102, 0.529, 0.183, and 0.21 nm/s, respectively, which were measured and confirmed with ellipsometry. The deposition parameters for each deposition materials in Helios are shown in Table I.

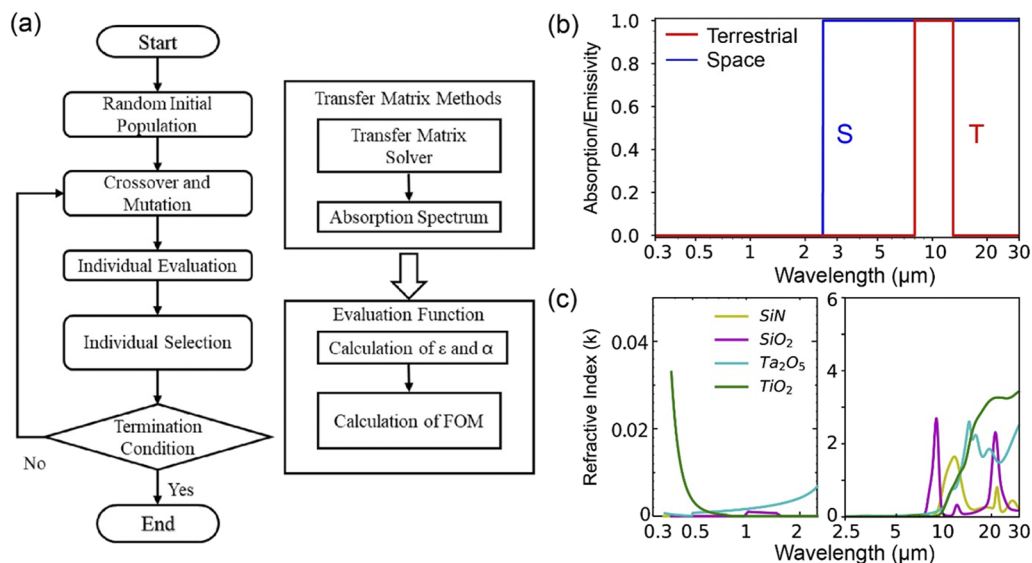


FIG. 1. (a) Flow chart of the genetic algorithm for OSR optimization using the transfer matrix method for the absorption spectrum calculation for the initial population and the following every new thickness and materials population. (b) Target absorption/emissivity spectrum for space and terrestrial application; the optimization range for the mid-infrared range is 2.5–30 and 8–13 μm . (c) Materials candidates for the optimization and its corresponding imaginary refractive index.

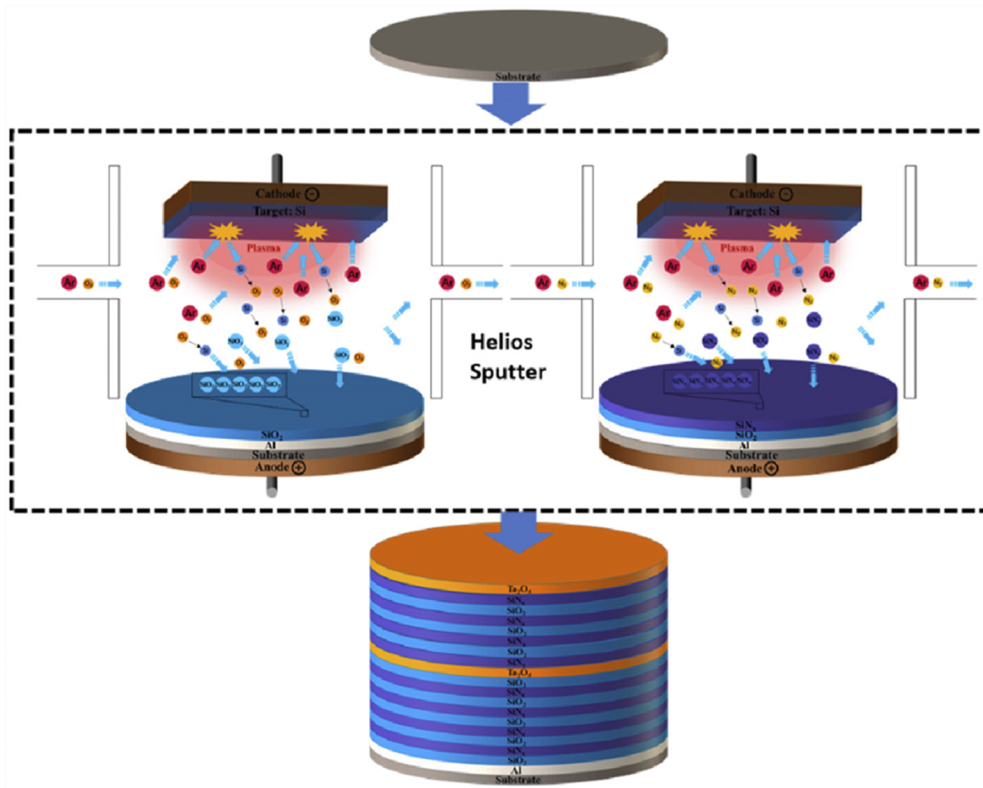


FIG. 2. Schematic of one-go manufacture of an optimized optical solar reflector with the Helios reactive sputtering tool.

TABLE I. Deposition parameters for the radiative cooler stack using Helios reactive sputtering.

Deposited materials	Targets	Power (W)	Pressure (mbar)	Gas	Gas flow (SCCM)
Ta ₂ O ₅	Ta	500	1 × 10 ⁻⁵	O ₂	30
SiN	Si	2000	1 × 10 ⁻⁵	N ₂	30
SiO ₂	Si	3000	1 × 10 ⁻⁵	Ar/O ₂	40/12
Al	Al	500	1 × 10 ⁻⁵	Ar	15

For the infrared emissivity measurement, an FTIR system (Thermo-Nicolet Nexus 670) with a DTGS detector was used to measure the reflectance from 6250 to 350 cm⁻¹ (equal to wavelength range from 1.6 to 28 μm). Angle dependence between 20° and 70° was measured using a variable-angle specular reflection accessory placed in the FTIR chamber. An uncoated gold film was used as a reference; all IR spectra were collected with an average 128 scans at room temperature. The solar absorptance in visible and near infrared was acquired through a total reflection spectrophotometer (Bentham PVE3000) with two reference detectors: silicon (0.3–1.0 μm) and germanium (1.0–1.8 μm), which is based on a supercontinuum xenon-quartz tungsten halogen dual light source over a range of 0.3–2.5 μm and an integrating sphere coated with BaSO₄; the reference for solar radiation measurement is using BaO₂.

III. RESULTS AND DISCUSSION

In the optimization, we consider two design scenarios, corresponding to a terrestrial radiative cooler (type T) with an optimized emissivity from 8 to 13 μm and a broadband space radiative cooler (type S) with an optimized emissivity from 2.5 to 30 μm with a target spectral response, as illustrated in Fig. 1(b). In the model, we allowed a set of four materials that are available for fabrication in our reactive sputtering tool (Helios), including SiO₂, SiN, TiO₂, and Ta₂O₅, with values of the imaginary part of the refractive index shown in Fig. 1(c).^{52,53} The genetic algorithm was able to select both the material and the thickness for each layer, with the goal of achieving the highest FOM ε/α over the spectral bandwidth of interest, where ε and α are normalized corresponding to the black-body radiation at 300 and 5777 K, respectively. The chosen materials all combine a low extinction in the solar absorption with a band

of high extinction in the infrared, the spectral range of the infrared absorption bands being different for the materials corresponding to their vibrational resonances. We, furthermore, assume that the emissivity equals the absorption in a thermodynamic equilibrium state following Kirchhoff's law of thermal radiation.

As an illustration of the optimization process, the Figure of Merit (FOM) with the number of generations of GA is presented in Fig. S1(c) for the case of the broadband radiative cooler for space. It is seen that the FOM converges at the 88th generation reaching the highest $\epsilon/\alpha = 10.2$. Very similar convergence was obtained for the terrestrial radiative cooler stacks (not shown). Results for the optimized multilayer stacks of both types are shown in Fig. 3, with the corresponding thermo-optical parameters presented in Table II. The optimized stack layouts and absorption spectra for the terrestrial (type T) and space (type S) radiative cooling stacks are plotted in Figs. 3(a) and 3(b). For the terrestrial cooler stack (type T), the model selected a multilayer consisting of two materials, SiN and SiO₂, which each has a high extinction coefficient in the wavelength range from 8 to 13 μm due to the existence of the absorption peak of Si-N bond stretching near 11.6 μm in SiN and Si-O bond stretching near 9.4 μm in SiO₂.⁵⁴ SiN and SiO₂ do not support a high absorption outside the 8–13 μm band (apart for a narrow absorption peak at 22.5 μm in SiO₂); therefore, the absorption tails off at longer wavelengths, typical for previously demonstrated terrestrial radiative coolers.^{13–18} Such a type-T radiative cooling device is particularly useful for sub-ambient radiative cooling on earth, but not for broadband cooling in space, with a broadband emissivity $\epsilon(2.5\text{--}30\text{ }\mu\text{m})$ of only 0.546 (see Table II).

For the broadband stack, the optimized design consists of three materials, SiN, SiO₂, and Ta₂O₅. The addition of Ta₂O₅ results in a strong improvement of the broadband absorption owing to its high extinction coefficient above 13 μm .⁵⁵ Ta₂O₅ is an inorganic

TABLE II. Thermo-optic parameters α and ϵ from design and fabrication stacks.

Substrate	Device	α (0.3–2.5 μm)	ϵ (2.5–30 μm)	ϵ/α
	Type T, calc	0.081	0.546	6.74
	Type S, calc	0.071	0.724	10.2
Silicon	Type T, expt.	0.112	0.624	5.57
	Type S, expt.	0.106	0.747	7.05
Kapton	Type S, expt.	0.130	0.75	5.77

compound with a high refractive index n of around 2.15 in the UV–visible, low absorption at a solar absorption range (0.3–2.5 μm) and high absorption at long wavelength infrared and far infrared, which has been widely used for optical coating with applications in antireflection and optical filter stacks.⁵² Detailed information on the layer structure of the type S stack is presented in Fig. S1(b) of the supplementary material. Here, it is worth mentioning that in both terrestrial and space cases, no TiO₂ is chosen in optimized design by GA, and this is attributed to its high imaginary refractive index in the visible range, as shown in Fig. 1(c), which can result in an undesirable visible absorption and lower FOM.

Figure 3(b) compares the simulated solar absorption of the optimized stacks with that of a single 100 nm Al reflector ($\alpha_{\text{Al-film}} = 0.078$). The spectra show a reduction of the solar absorption of the type S stack below that of a plane Al film, which indicates that the “periodic-like” structures generated by GA act as distributed Bragg reflector structures. These structures can selectively reflect visible spectra, thereby mitigating the residual losses of the Al mirror

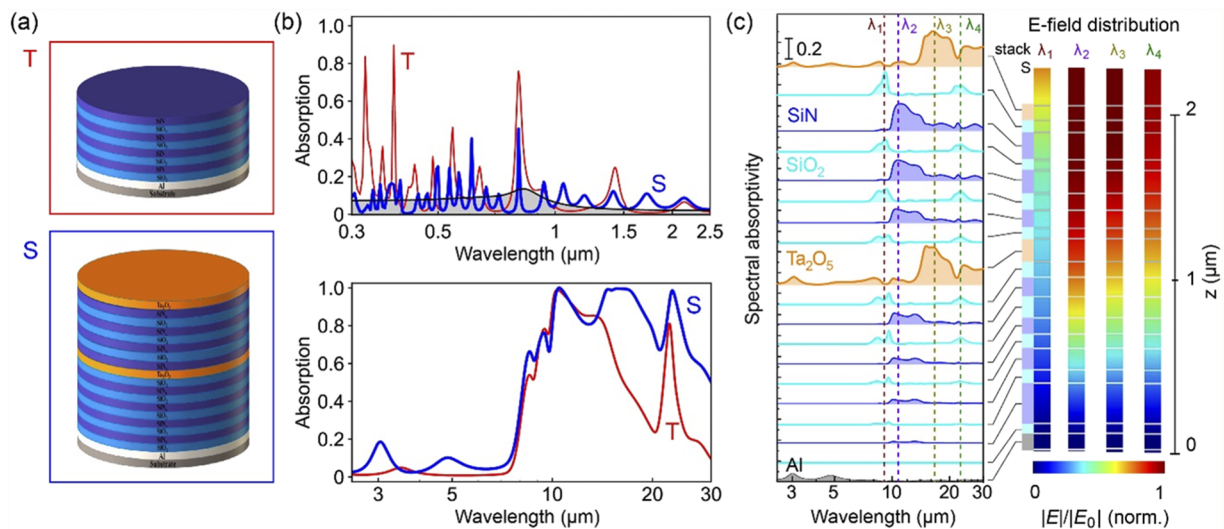


FIG. 3. (a) Schematic of the optimized OSR stacks for terrestrial (T) and space (S) applications. Type T consists of eight layers of SiO₂ and SiN, and type S consists of 18 alternating layers of Ta₂O₅, SiO₂, and SiN on the Al mirror. (b) Calculated UV–visible and infrared absorption spectra of the two OSR types T and S compared to the Al film (black line). (c) Calculated absorption contributions from each layer of type S and electric (E-)field intensity for intrinsic absorption at 9.46, 10.22, 16.5, and 22.5 μm wavelengths.

itself. The improved performance of type S over type T, consistently seen in calculated and experimental α values, can be attributed to the improved UV–visible reflectivity from the additional layers and the high refractive index contrast offered by the Ta₂O₅ layers. With respect to the choice of a metal backreflector, we, furthermore, note that both Ag and Al films are good candidates for achieving a good visible, near-IR, and mid-IR reflectance with generally Ag-based designs offering a reduced solar absorption (see Table S1 in the supplementary material). The motivation of using Al in our model is based on the durability of Al against oxidation both in the reactive sputtering process as well as in the space environment (e.g., atomic oxygen exposure in low-earth orbit), compared to Ag.

To elucidate the absorption contribution from each layer in broadband cooler stack S, we calculated the spectral absorptivity of each of the designed layers in the stack, as shown in Fig. 3(c). Similar results for terrestrial stack i are shown in Fig. S2 of the supplementary material. Figure 3(c) shows that the top 10 layers contribute the strongest to the infrared absorption, whereas the absorption in the underlying layers decreases as we get closer to the Al backreflector. This can be understood from basic principles, as the device approximates a $\lambda/4$ perfect absorber (Salisbury) screen, where the electric field has a node at the backreflector (ground plane) and a maximum absorption is obtained at a quarter wavelength distance away from the mirror. For traditional infrared perfect absorbers aimed at controlling blackbody radiation at room temperature using a single, thin-film or metasurface absorption layer, typically the optimum distance for achieving maximum absorption is around 1 μm .³² For a distributed multilayer stack, such as presented in this study,

different parts of the spectrum will be preferably absorbed at different depths in the stack, while for all wavelengths, absorption decreases for distances close to the mirror as the standing-wave electric field approaches the node at the mirror surface. Figure 3(c) shows the electric (E -)field distribution in the absorbing stack at four selected wavelengths corresponding to particular absorption features of the different materials at $\lambda_1 = 9.46 \mu\text{m}$ (SiO₂), $\lambda_2 = 10.22 \mu\text{m}$ (SiN), $\lambda_3 = 16.5 \mu\text{m}$ (Ta₂O₅), and $\lambda_4 = 22.5 \mu\text{m}$ (both SiO₂ and Ta₂O₅). For λ_2 to λ_4 , we see that the penetration of the wave into the stack is increasingly reduced toward longer wavelengths, whereas the wave at λ_1 is strongly attenuated already in the first few SiO₂ layers.

The as-optimized radiative cooling devices were fabricated using the Helios reactive sputtering tool using a one-go, single step fabrication process. For the amorphous Ta₂O₅ thin layers, a post-anneal step in air at 450 °C was required to further improve the stoichiometry via oxidation,⁵⁶ resulting in a significant improvement of the optical transparency in the visible range (see Fig. S3 in the supplementary material). The fabricated 150 mm (6 in.) OSR wafers are represented in Figs. 4(a) and 4(b) with corresponding experimental absorption spectra in Fig. 4(d). Figure 4(e) represents the cross-sectional scanning electron microscopy (SEM) image of the broadband radiative cooler stack, showing the approximate thickness of the individual layers in the stack via the electron backscattering contrast of the different materials.

The optical photographs in Fig. 4 illustrate the reflective characteristics of the samples in the visible, which is characterized by low solar absorption when integrated from 0.3 to 2.5 μm and reflection of over 89% of the incident solar power, owing to the high reflectance

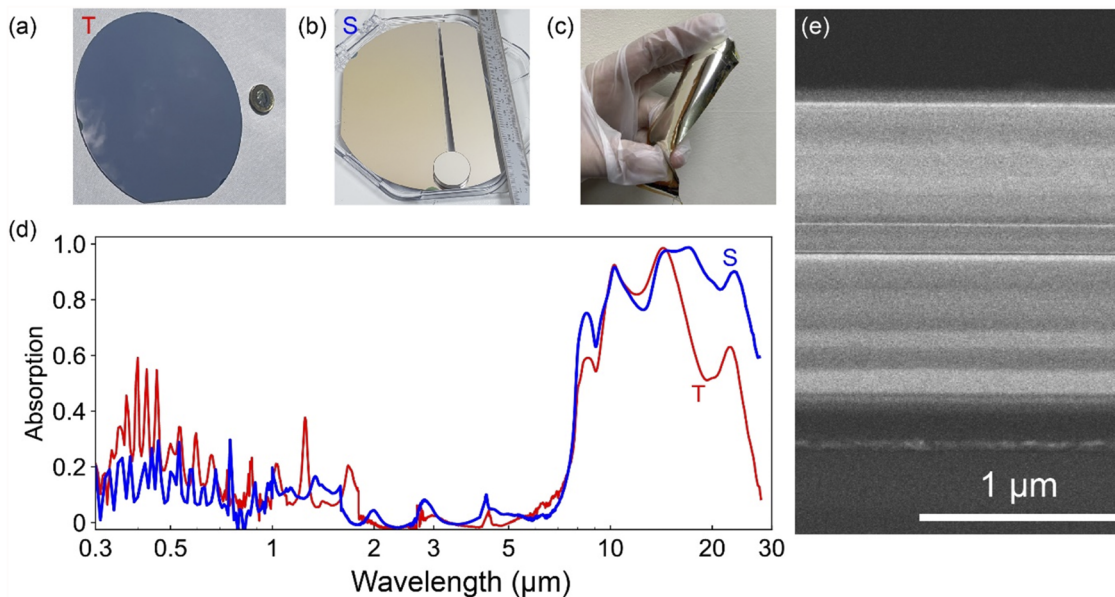


FIG. 4. Experimental 150 mm diameter radiative coolers fabricated on silicon (a) and (b) and polyimide foil (c) for terrestrial type T (a) and broadband space type S (b) and (c). (d) Experimental absorption spectrum for type T, S samples from (a) and (b). (e) Cross-sectional SEM from the broadband radiative cooler sample from (b). Terrestrial cooler photograph (a) was taken in outdoor ambient conditions, showing reflection from the sky. A broadband cooler (b) image taken under laboratory illumination, showing unannealed (left) and annealed (right) sections (see also Fig. S3), protected Al mirror (Thorlabs) shown for comparison.

of the Al mirror and the low optical losses of SiO₂, SiN, and Ta₂O₅ within the solar range. The spectral response of the fabricated OSRs in Fig. 4(d) also shows a high emissivity in the mid-infrared due to the high extinction coefficient of SiO₂, SiN, and Ta₂O₅. The experimental spectra match well with the simulations of Fig. 3, where a slight difference in the visible range attributed to an imperfect annealing of the middle Ta₂O₅ layer in the stack, due to dense SiN layers blocking the O₂ diffusion. The thermo-optical coefficients of the experimental devices are summarized in Table II. Overall, the as-fabricated S type OSR shows good thermal-optical properties with $\alpha = 0.106$, $\epsilon = 0.747$ (2.5–30 μm), and $\epsilon/\alpha = 7.05$.

The same design for the broadband cooler stack of type S has also been applied on a flexible 80 × 30 mm² Kapton substrate by using the same sputter deposition process. An optical photograph of the as-fabricated flexible OSR is shown in Fig. 4(c). Full results are shown in Fig. S4 comparing the absorption of multilayer OSR fabricated on a silicon substrate and flexible polyimide substrate (Kapton foil); the absorption spectra are quite similar, and the flexible multilayer OSR also shows promising thermal-optical properties with $\alpha = 0.13$, $\epsilon = 0.75$ (2.5–30 μm), and $\epsilon/\alpha = 5.77$. The limited thermal budget of the Kapton foil prevented a similar post-anneal to improve a performance, and future work is needed to further optimize the deposition process to reduce the post-anneal requirements. Good agreement for the as deposited samples indicates that, in principle, the thin-film stacks are compatible with flexible substrates.

Figure 5 shows the dependence of emissivity on angle for the two types of OSR. Figure 5(a) shows the experimental infrared absorption against angle of incidence; polar plots are shown in Fig. 5(b) for both the emissivity and the solar absorbance. Infrared emissivity ($\epsilon > 0.70$) of the OSR persists to a large angle of incidence up to 50° and remains high ($\epsilon > 0.66$) even at an angle of incident of 60°, which is important for maximizing the total radiated power

over all angles (hemispherical emissivity). The solar absorbance α remains below 0.10 up to a large angle of incidence at 85° for both designs.

The experimental thermo-optical parameters can be used to estimate the cooling capabilities of the thin-film OSRs. For this purpose, we consider a space environment with a total solar irradiance of one sun (1.26 kW/m²) at normal incidence, which for $\alpha = 0.106$ results in a solar heating of 134.0 W/m², a radiative cooling of 284.1 W/m², and hence a net cooling of 150.1 W/m². The radiative cooling power is about 73% of the theoretical maximum of 387 W/m². The calculation method is detailed in our previous work.³⁷ To get some insights of its performance, we compare it with two commercial products, conventional standard glass-tile OSR by Qioptic (Excelitas Technology) and novel flexible OSR (Interferential CERMET) by Consorzio CREO. The net radiative cooling is calculated to be 207 and 184 W/m² for standard OSR and flexible OSR, respectively. The superior performance for these two OSRs is attributed to their higher IR emissivity of 0.86 and 0.8, respectively. Currently, the maximum emissivity of the stacks is limited by the sharp drop of emissivity below 8 μm , which is caused by the lack of inorganic optical materials with a sufficiently high extinction coefficient in the spectral range of 2.5–8 μm that are simultaneously transparent in the visible range. We identify some notable exceptions, in particular transparent conductive oxide.³² As shown in Fig. S5, the IR emissivity also depends on surface temperature as the blackbody emission peak blueshifts with temperature increase, leading to a performance degradation at elevated temperature. Therefore, it would be critical to integrate the transparent conductive oxide to extend the emissivity at shorter wavelengths below 8 μm and further improve the IR emissivity. In this work, we focused our discussion on broadband radiative cooling for space applications. However, the developed structures are equally useful for above-ambient cooling in the terrestrial environment.⁵⁸

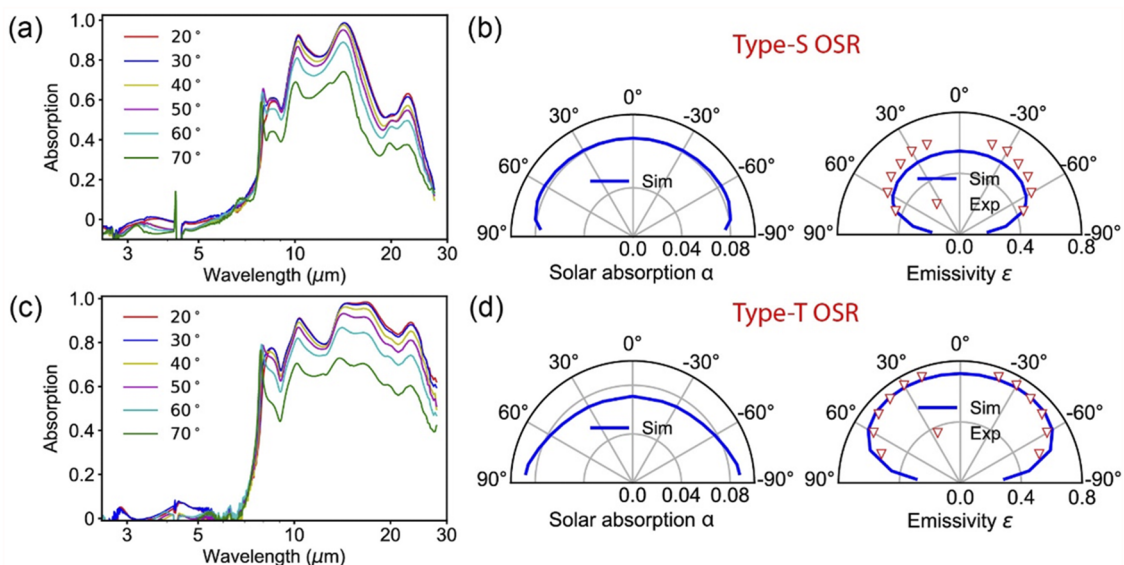


FIG. 5. Experimental infrared absorption against angle for terrestrial type T (a) and broadband space type S (c). (b) and (d) Angle-dependence of solar absorption α (0.3–2.5 μm) and broadband emissivity ϵ (2.5–28 μm) for simulations (blue lines) and experimental data (red triangles).

Most works on terrestrial applications focus on the spectral range 8–13 μm , the infrared atmosphere transmission windows suitable for sub-ambient radiative cooling.^{22,59}

Compared with previous thin film radiative cooling works⁶⁰ either inorganic on a solid silicon/glass substrate^{22,47,61,62} or organic polymers,^{63,64} this work demonstrates novelty in different aspects: First, by introducing standard optical material Ta_2O_5 as the ideal material to extend the long-wave infrared bandwidth of the emissivity to above 25 μm . Second, by using an optimized design with as many as 18 layers, we achieve excellent thermo-optical performance using an ultra-thin stack. Finally, the integration of the film OSR on a polyimide substrate is desirable for applications in both terrestrial and space for its low weight, easy assembly, and conformal adaptation to curved surfaces, which can significantly reduce launch and assembly cost of spacecraft. In addition, the selected materials are inorganic and durable and robust in the operation temperature range and have no degassing issues.

IV. CONCLUSION

In conclusion, the genetic algorithm combined with transfer matrix methods was successfully applied to the optimization of a thin-film-based optical solar reflector with broadband infrared emissivity and low solar absorption. The optimized design consists of 18 layers of SiN, SiO₂, and Ta₂O₅ on an aluminum mirror with a total thickness of 2.088 μm and a figure of merit of $\epsilon/\alpha = 10.2$. The as-designed thin-film-based OSR was fabricated onto a 150 mm Si substrate and a flexible Kapton substrate using industrial-level sputter equipment compatible with future mass production. The fabricated OSR showed an infrared emissivity of $\epsilon = 0.75$ in the broadband infrared range (2.5–30 μm) and exhibited an absorption of $\alpha = 0.11$ in the solar window (0.3–2.5 μm), which shows a highly selective optical property for the radiative cooling of space applications, with a net cooling power of 150.1 W/m². The thin-film inorganic material based OSR foil provides a lightweight, low fabrication cost, flexible, and high film quality strategy to replace the current OSR design for space-based applications, such as thermal management of spacecraft and light sails.

SUPPLEMENTARY MATERIAL

See the supplementary material for additional information, including (i) calculation of thermal-optical properties and (II) design and fabrication of a terrestrial radiative cooler.

ACKNOWLEDGMENTS

O.L.M. and K.S. acknowledge the support from EPSRC through an Impact Acceleration Account project. The authors acknowledge the support from DuPont for freely providing DuPont Kapton[®] PFC 300 as polyimide substrates.

AUTHOR DECLARATIONS

Conflict of Interest

The authors have no conflicts to disclose.

Author Contributions

W.X. and P.D. contributed equally to this work.

Wei Xiao: Conceptualization (equal); Data curation (equal); Formal analysis (equal); Investigation (equal); Software (equal); Writing – original draft (equal). **Peng Dai:** Investigation (equal); Methodology (equal); Software (equal); Validation (equal); Writing – review & editing (supporting). **H. Johnson Singh:** Investigation (equal); Software (equal). **Idris A. Ajia:** Investigation (supporting); Methodology (supporting). **Xingzhao Yan:** Methodology (supporting); Resources (supporting). **Peter R. Wiecha:** Methodology (supporting); Software (supporting); Writing – review & editing (supporting). **Ruomeng Huang:** Methodology (supporting); Supervision (supporting); Writing – review & editing (supporting). **C. H. (Kees) de Groot:** Conceptualization (equal); Funding acquisition (supporting); Investigation (supporting); Methodology (supporting); Project administration (supporting); Supervision (equal); Writing – review & editing (supporting). **Otto L. Muskens:** Conceptualization (equal); Data curation (equal); Formal analysis (equal); Funding acquisition (equal); Investigation (equal); Methodology (equal); Project administration (equal); Supervision (equal); Visualization (equal); Writing – review & editing (equal). **Kai Sun:** Conceptualization (equal); Data curation (equal); Formal analysis (equal); Funding acquisition (equal); Investigation (equal); Methodology (equal); Project administration (equal); Software (equal); Supervision (equal); Writing – original draft (equal); Writing – review & editing (equal).

DATA AVAILABILITY

The data that support the findings of this study are openly available in the University of Southampton repository at <http://doi.org/10.5258/SOTON/D2602>.

REFERENCES

- H. A. Atwater, A. R. Davoyan, O. Ilic, D. Jariwala, M. C. Sherrott, C. M. Went, W. S. Whitney, and J. Wong, *Nat. Mater.* **17**(10), 861 (2018).
- A. R. Davoyan, J. N. Munday, N. Tabiryan, G. A. Swartzlander, and L. Johnson, *Optica* **8**(5), 722 (2021).
- O. Ilic, C. M. Went, and H. A. Atwater, *Nano Lett.* **18**(9), 5583 (2018).
- Z. Chen, L. Zhu, W. Li, and S. Fan, *Joule* **3**(1), 101 (2019).
- V. L. Pisacane, *Fundamentals of Space Systems* (Johns Hopkins University, 2005).
- M. Hołyńska, A. Tighe, and C. Semprimoschnig, *Adv. Mater. Interfaces* **5**(11), 1701644 (2018).
- S. Tachikawa, H. Nagano, A. Ohnishi, and Y. Nagasaka, *Int. J. Thermophys.* **43**(6), 91 (2022).
- E. Miyazaki, J. Ishizawa, and H. Shimamura, in *Proceedings of International Symposium on "SM/MPAC and SEED Experiment"* JAXA-SP-08-015E (JAXA, 2009), p. 149.
- K. N. Marshall and R. A. Breuch, *J. Spacecr. Rockets* **5**(9), 1051 (1968).
- M. Moser, C. Ranzenberger, and S. Duzellier, paper presented at the 46th International Conference on Environmental Systems, 2016 (unpublished).
- B. Putz, S. Wurster, T. E. J. Edwards, B. Völker, G. Milassin, D. M. Többens, C. O. A. Semprimoschnig, and M. J. Cordill, *Acta Astronaut.* **175**, 277 (2020).
- J. A. Townsend, P. A. Hansen, J. A. Dever, K. K. de Groh, B. A. Banks, L. Wang, and C. He, *High Perform. Polym.* **11**(1), 81 (1999).
- D. Zhao, A. Aili, Y. Zhai, S. Xu, G. Tan, X. Yin, and R. Yang, *Appl. Phys. Rev.* **6**(2), 021306 (2019).
- J. Chen and L. Lu, *Sol. Energy* **212**, 125 (2020).

- ¹⁵X. Yin, R. Yang, G. Tan, and S. Fan, *Science* **370**(6518), 786 (2020).
- ¹⁶R. Hu, Y. Liu, S. Shin, S. Huang, X. Ren, W. Shu, J. Cheng, G. Tao, W. Xu, and R. Chen, *Adv. Energy Mater.* **10**(17), 1903921 (2020).
- ¹⁷J. Liu, Z. Zhou, J. Zhang, W. Feng, and J. Zuo, *Mater. Today Phys.* **11**, 100161 (2019).
- ¹⁸B. Zhao, M. Hu, X. Ao, Q. Xuan, and G. Pei, *Appl. Energy* **262**, 114548 (2020).
- ¹⁹A. P. Raman, M. A. Anoma, L. Zhu, E. Rephaeli, and S. Fan, *Nature* **515**(7528), 540 (2014).
- ²⁰E. Rephaeli, A. Raman, and S. Fan, *Nano Lett.* **13**(4), 1457 (2013).
- ²¹C. Zou, G. Ren, Md M. Hossain, S. Nirantar, W. Withayachumnankul, T. Ahmed, M. Bhaskaran, S. Sriram, M. Gu, and C. Fumeaux, *Adv. Opt. Mater.* **5**(20), 1700460 (2017).
- ²²M. M. Hossain, B. Jia, and M. Gu, *Adv. Opt. Mater.* **3**(8), 1047 (2015).
- ²³B. Bhatia, A. Leroy, Y. Shen, L. Zhao, M. Gianello, D. Li, T. Gu, J. Hu, M. Soljačić, and E. N. Wang, *Nat. Commun.* **9**(1), 5001 (2018).
- ²⁴K. Tang, K. Dong, J. Li, M. P. Gordon, F. G. Reichertz, H. Kim, Y. Rho, Q. Wang, C.-Y. Lin, C. P. Grigoropoulos, A. Javey, J. J. Urban, J. Yao, R. Levinson, and J. Wu, *Science* **374**(6574), 1504 (2021).
- ²⁵W. Li, Y. Shi, K. Chen, L. Zhu, and S. Fan, *ACS Photonics* **4**(4), 774 (2017).
- ²⁶L. Zhu, A. Raman, K. X. Wang, M. A. Anoma, and S. Fan, *Optica* **1**(1), 32 (2014).
- ²⁷S. Wang, T. Jiang, Y. Meng, R. Yang, G. Tan, and Y. Long, *Science* **374**(6574), 1501 (2021).
- ²⁸S. Mengali, M. Simeoni, A. Urbani, L. Mapelli, C. Sabato, R. Heflin, and G. Çorapcıoğlu, in *Proceedings of the 14th ISMSE and 12th ICPMSE* (IOP Publishing, Biarritz, 2018).
- ²⁹S. Loke, A. Naqavi, E. Warmann, P. Espinet-Gonzalez, N. Vaidya, M. Kelzenberg, and H. A. Atwater, *Opt. Express* **30**(16), 28268 (2022).
- ³⁰M. Benkahoul, M. Chaker, J. Margot, E. Haddad, R. Kruzelecky, B. Wong, W. Jamroz, and P. Poinas, *Sol. Energy Mater. Sol. Cells* **95**(12), 3504 (2011).
- ³¹A. Hendaoui, N. Émond, M. Chaker, and É. Haddad, *Appl. Phys. Lett.* **102**(6), 061107 (2013).
- ³²K. Sun, C. A. Riedel, Y. Wang, A. Urbani, M. Simeoni, S. Mengali, M. Zalkovskij, B. Bilenberg, C. H. de Groot, and O. L. Muskens, *ACS Photonics* **5**(2), 495 (2018).
- ³³J. Mandal, Y. Fu, A. C. Overvig, M. Jia, K. Sun, N. N. Shi, H. Zhou, X. Xiao, N. Yu, and Y. Yang, *Science* **362**(6412), 315 (2018).
- ³⁴Y. Zhai, Y. Ma, S. N. David, D. Zhao, R. Lou, G. Tan, R. Yang, and X. Yin, *Science* **355**(6329), 1062 (2017).
- ³⁵O. Ilic, *MRS Bull.* **45**(9), 769 (2020).
- ³⁶K. Sun, C. A. Riedel, A. Urbani, M. Simeoni, S. Mengali, M. Zalkovskij, B. Bilenberg, C. H. de Groot, and O. L. Muskens, *ACS Photonics* **5**(6), 2280 (2018).
- ³⁷E. Haddad, R. V. Kruzelecky, A. Hendaoui, M. Chaker, W. Jamroz, and P. Poinas, paper presented at the 43rd International Conference on Environmental Systems, 2013 (unpublished).
- ³⁸A. Naqavi, S. P. Loke, M. D. Kelzenberg, D. M. Callahan, T. Tiwald, E. C. Warmann, P. Espinet-González, N. Vaidya, T. A. Roy, J.-S. Huang, T. G. Vinogradova, and H. A. Atwater, *Opt. Express* **26**(14), 18545 (2018).
- ³⁹P. R. Wiecha, A. Arbouet, C. Girard, A. Lecestre, G. Larriue, and V. Paillard, *Nat. Nanotechnol.* **12**(2), 163 (2017).
- ⁴⁰S. Molesky, Z. Lin, A. Y. Piggott, W. Jin, J. Vucković, and A. W. Rodriguez, *Nat. Photonics* **12**(11), 659 (2018).
- ⁴¹T. Feichtner, O. Selig, M. Kiunke, and B. Hecht, *Phys. Rev. Lett.* **109**(12), 127701 (2012).
- ⁴²K. Yao, R. Unni, and Y. Zheng, *Nanophotonics* **8**(3), 339 (2019).
- ⁴³G. J. Lee, Y. J. Kim, H. M. Kim, Y. J. Yoo, and Y. M. Song, *Adv. Opt. Mater.* **6**(22), 1800707 (2018).
- ⁴⁴Z. Chen, L. Zhu, A. Raman, and S. Fan, *Nat. Commun.* **7**(1), 13729 (2016).
- ⁴⁵H. Ma, K. Yao, S. Dou, M. Xiao, M. Dai, L. Wang, H. Zhao, J. Zhao, Y. Li, and Y. Zhan, *Sol. Energy Mater. Sol. Cells* **212**, 110584 (2020).
- ⁴⁶P. You, X. Li, Y. Huang, X. Ma, M. Pu, Y. Guo, and X. Luo, *Materials* **13**(13), 2885 (2020).
- ⁴⁷D. Chae, M. Kim, P.-H. Jung, S. Son, J. Seo, Y. Liu, B. J. Lee, and H. Lee, *ACS Appl. Mater. Interfaces* **12**(7), 8073 (2020).
- ⁴⁸S. Y. Jeong, C. Y. Tso, J. Ha, Y. M. Wong, C. Y. H. Chao, B. Huang, and H. Qiu, *Renewable Energy* **146**, 44 (2020).
- ⁴⁹Y. Shi, W. Li, A. Raman, and S. Fan, *ACS Photonics* **5**(3), 684 (2017).
- ⁵⁰F. M. De Rainville, F. A. Fortin, M. A. Gardner, M. Parizeau, and C. Gagné, “DEAP: Evolutionary algorithms made easy,” *J. Mach. Learn. Res.* **13**(1), 2171 (2012).
- ⁵¹X.-S. Yang, *Nature-inspired Optimization Algorithms* (Academic Press, 2020).
- ⁵²T. J. Bright, J. I. Watjen, Z. M. Zhang, C. Muratore, A. A. Voevodin, D. I. Koukis, D. B. Tanner, and D. J. Arenas, *J. Appl. Phys.* **114**(8), 083515 (2013).
- ⁵³J. Kischkat, S. Peters, B. Gruska, M. Semtsiv, M. Chashnikova, M. Klinkmüller, O. Fedosenko, S. Machulik, A. Aleksandrova, G. Monastyrskiy, Y. Flores, and W. Ted Masselink, *Appl. Opt.* **51**(28), 6789 (2012).
- ⁵⁴S. Zhou, W. Liu, C. Cai, and H. Liu, paper presented at the Seventh International Conference on Thin Film Physics and Applications, 2011 (unpublished).
- ⁵⁵H. Ono and K.-i. Koyanagi, *Appl. Phys. Lett.* **77**(10), 1431 (2000).
- ⁵⁶J. S. Lee, S.-J. Chang, J.-F. Chen, S. C. Sun, C. H. Liu, and U. H. Liaw, *Mater. Chem. Phys.* **77**(1), 242 (2003).
- ⁵⁷K. Sun, W. Xiao, C. Wheeler, M. Simeoni, A. Urbani, M. Gaspari, S. Mengali, C. H. de Groot, and O. L. Muskens, *Nanophotonics* **11**(17), 4101 (2022).
- ⁵⁸P. Li, A. Wang, J. Fan, Q. Kang, P. Jiang, H. Bao, and X. Huang, *Adv. Funct. Mater.* **32**(5), 2109542 (2022).
- ⁵⁹J.-I. Kou, Z. Jurado, Z. Chen, S. Fan, and A. J. Minnich, *ACS Photonics* **4**(3), 626 (2017).
- ⁶⁰S. Wu, Y. Cao, Y. Li, and W. Sun, *Adv. Opt. Mater.* **11**(4), 2202163 (2023).
- ⁶¹D. U. Yildirim, A. Ghobadi, M. C. Soydan, O. Atesal, A. Toprak, M. D. Caliskan, and E. Ozbay, *ACS Photonics* **6**(7), 1812 (2019).
- ⁶²F. B. Barho, F. Gonzalez-Posada, L. Cerutti, and T. Taliercio, *Adv. Opt. Mater.* **8**(6), 1901502 (2020).
- ⁶³L. Zhou, J. Zhao, H. Huang, F. Nan, G. Zhou, and Q. Ou, *ACS Photonics* **8**(11), 3301 (2021).
- ⁶⁴Y. Gao, X. Song, A. S. Farooq, and P. Zhang, *Sol. Energy* **228**, 474 (2021).